

# Study of the effect of SLM energy density on residual stress and microstructure of porous bone scaffolds in cubic structures

Sen Zhang<sup>1</sup>, Shubo Xu<sup>1,2,\*</sup> , Wei Zheng<sup>1</sup>, and Juanjuan Han<sup>1</sup>

<sup>1</sup> School of Materials Science and Engineering, Shandong Jianzhu University, Jinan 250101, China

<sup>2</sup> State Key Laboratory of Materials Processing and Die & Mould Technology, Huazhong University of Science and Technology, Wuhan 430074, China

Received: 20 September 2022 / Accepted: 17 October 2022

**Abstract.** In order to investigate the effect of energy density in selective laser melting (SLM) forming on the properties of porous bone scaffolds made of 316L stainless steel, the mechanism of different construction energy densities on the residual stress and microstructure of cubic porous bone scaffolds was investigated by combining experiments and finite element analysis. The results showed that many defects were formed in the scaffolds when too high or too low energy densities were used to form the porous bone scaffolds. In terms of microstructure, inappropriate energy densities caused some grains to appear coarse and dispersed, which directly led to a reduction in the corrosion resistance of the scaffolds. Most importantly, the stress and temperature field changes in the melt pool during the SLM forming process were obtained through finite element calculations and analysis, and it was found that the residual stress in the scaffolds was proportional to the energy density. After a comprehensive study of the finite element analysis results and experimental characterization, the optimum energy density for constructing cubic porous bone scaffolds with ideal defects and residual stress in the porous bone scaffolds was obtained.

**Keywords:** Porous bone scaffolds / selected laser melting / residual stress / microstructure / finite element analysis

## 1 Introduction

316L stainless steel is widely used in biomedical, chemical, and light industrial applications due to its excellent properties [1,2]. In the area of medical implants and bone repair materials, traditional solid 316L stainless steel implants suffer from a “stress shielding” effect, which can easily lead to implant failure. In recent years, in order to enhance the biomechanical properties and bone regeneration of artificial implants, many researchers have designed porous scaffolds and conducted numerous experimental applications with significant results. It has been found that the use of additive manufacturing is one of the most efficient ways of forming porous scaffolds, but there are still many challenges to overcome before SLM can become a widely accepted and adopted technology in biomedical manufacturing.

Through research, it is found that SLM technology directly carries out metal sintering, which can usually introduce a steep temperature gradient, and with the rapid

solidification of the molten pool, the uneven microstructure will be generated [3]. Wauthle [4] and others found through research that after SLM forming, necessary measures should be taken to reduce or remove the impact of residual stress to improve the performance of SLM parts. In addition, the processing characteristics of SLM make it easy to produce uneven forming quality in the formed parts, which leads to performance differences. In the SLM process, because the molten pool exists for a short time, the fluidity of molten metal is greatly reduced, and warping deformation, tensile residual stress, porosity, and unmelted powder are inevitable in the formed parts [5–7]. Wei et al. [8] obtained through research, reducing or avoiding the intersection of incident lasers during processing can reduce the defects in the formed parts, thus improving the mechanical properties. However, defects in the SLM process are unavoidable. What we can do is minimize the occurrence of defects and form products with high quality. Tsopanos et al. [9] have studied that changing SLM process parameters, laser power and laser exposure time has an important impact on the mechanical properties of the lattice structure. Rehme et al. [10] studied and obtained the influence of laser parameters on the

\* e-mail: [xsbsdjzu.edu.cn](mailto:xsbsdjzu.edu.cn)

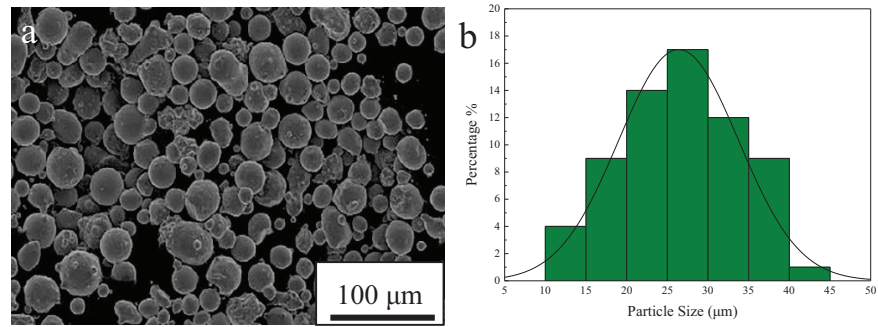


**Fig. 1.** SEM image (a) and particle size distribution (b) of 316L powder.

realization of various configurations of microcrystalline lattice structures. Zhang et al. [11] found that the choice of different energy densities can have a huge difference in the direction of grain growth in the molten pool, thus affecting the performance of the scaffold. In addition, the laser with low energy density is more suitable for the construction of porous bone scaffolds. As for the residual stress of SLM forming, many scholars have given roughly the same view, that is, the laser energy density has the most obvious impact on the residual stress inside the workpiece. Wang [12] and others found that rapid solidification and repeated thermal cycles of materials will lead to the accumulation of residual stress, which will lead to part deformation and have a negative impact on the mechanical properties of the parts, Mercelis et al. [13] found that the generation of residual stress can be better controlled and the forming can be optimized by controlling the energy density and forming angle. Mahyar et al. [14] found that material characteristics, sample and substrate height, laser scanning strategy, and heating conditions were the most important parameters to determine the size and shape of residual stress distribution. Xu et al. [15] found that low energy density should be selected for processing when building the porous bone scaffolds with body centered cubic structure, thus obtaining low residual stress and good material properties. At the same time, some scholars believe that the residual stress of SLM forming can improve some of the corrosion resistance of the workpiece. For example, Ali [16] and others elaborated that process parameters have different effects on the corrosion performance of additive manufacturing (AM) parts by affecting the microstructure characteristics of AM parts. Cruz [17] studied that the compressive residual stress in SLM forming parts can improve the pitting resistance of 316L parts.

Although SLM may have some defects and residual stress, it is still an advanced technology in material processing and medical applications. The research found that the performance improvement of the parts formed by AM in the original state or after simple post-processing in bone tissue engineering applications [18], material compressive properties, and elastic modulus [19] is far greater than that of the samples formed by traditional manufacturing methods, which makes the artificial porous bone scaffolds

made of AM more and more popular in the medical field. However, most of the existing studies focus on the biomechanical properties of porous bone scaffolds [20,21] and the optimization of porous structures [22,23]. The diversity of porous bone scaffolds structure makes us have to consider whether the construction parameters, construction stress, and residual deformation will affect the performance of the scaffolds in all aspects and whether the porous bone scaffolds with different structures in SLM construction needs to match specific energy density processing, etc. Therefore, in this study, it was decided to take different processing energy densities as the starting point, combined with finite element and experimental methods, to study the effects of different construction energy densities choices on various aspects of the performance of the porous scaffolds of cubic structure, and summarize its rules to provide a theoretical basis for the construction of porous scaffolds of other structures.

## 2 Materials and methods

### 2.1 Materials and equipment

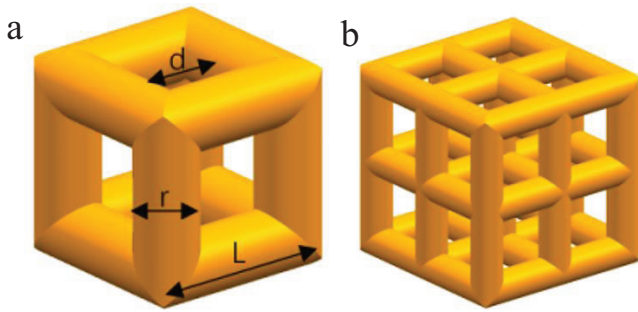
The experimental powder was made from 316L stainless steel powder (AVIC METE, China) by Argon atomisation method, with powder diameters ranging from 15 to 53 μm and an average particle size of 27 μm. Figure 1 shows SEM picture of 316L powder and the particle size distribution. The forming equipment used for the experiments was an FS121M machine manufactured by Huashu Hi-Tech, China.

### 2.2 Selection of the experimental protocol

In this study, energy density is an important factor to be considered in the optimization of parameters. Therefore, in this study, according to the experimental equipment and the research results of many scholars at home and abroad, it was decided to set the energy density initially between 40 and 120 J/mm<sup>3</sup>. The energy density of the selected was mainly determined by the laser power, scanning speed, hatching spacing, and powder thickness. The specific mathematical model is shown in equation (1), where  $P$  is the laser power (W),  $v$  is the laser scanning speed,  $s$  is the laser hatching spacing and  $t$  is the thickness of each layer of

**Table 1.** Orthogonal parameter design.

Experimental programme	Laser power $P$ (W)	Scanning speed $V$ (mm/s)	Hatching spacing $S$ (mm)	Energy density $E$ (J/mm <sup>3</sup> )
1#	100	500	0.06	83.3
2#	100	600	0.10	41.7
3#	100	700	0.08	44.6
4#	130	500	0.10	65.0
5#	130	600	0.08	67.7
6#	130	700	0.06	77.4
7#	160	500	0.08	100.0
8#	160	600	0.06	111.1
9#	160	700	0.10	57.1

**Fig. 2.** Cubic porous scaffold: (a) Cube element; (b) Additive analysis model.

powder. The laser power was chosen to be between 100 W and 160 W, the hatching spacing was 0.06–0.10 mm, the scanning speed was between 500 and 700 mm/s and the thickness of each layer of powder was set to 0.04 mm to construct the porous bone scaffolds [22–24], and the specific experimental protocol is shown in Table 1.

$$E = \frac{p}{vst}. \quad (1)$$

### 2.3 Model of the scaffolds

The cubic structure was selected as the unitary structure of the porous bone scaffold for the study. The cubic structure is shown in Figure 2a, using a unitary structure with a porosity of 65% and a pore size of 800  $\mu\text{m}$  [25–27]. The specific structural design parameters are shown in Table 2.

### 2.4 Finite element analysis

Two softwares, Additive and Welding in Simufact, were used to simulate the additive manufacturing process and molten pool of the porous structure scaffolds. Simufact additive adopts the system adaptive hexahedral mesh generation. Under this mesh generation condition, the number of internal and boundary voxels is 63564 and 21866 respectively. As shown in Figure 2b, the Simufact additive model is  $2 \times 2 \times 2$  unit.

The Simufact Additive software is based on the inherent strain theory for finite element calculations. The software can analyse and calculate the generation and distribution of stress and deformations within the support during the forming process. SLM processing is a complex melt and solidification process, and the deformation and strain at any point in SLM additive manufacturing are related as follows.

$$\varepsilon = \varepsilon_e + \varepsilon_p + \varepsilon_T + \varepsilon_x, \quad (2)$$

where  $\varepsilon_e$  is the elastic strain,  $\varepsilon_p$  is the plastic strain,  $\varepsilon_T$  is the thermal strain and  $\varepsilon_x$  is the phase change strain. The intrinsic strain is defined as the sum of the plastic strain  $\varepsilon_p$ , the thermal strain and the corresponding change, i.e.

$$\varepsilon^* = \varepsilon_p + \varepsilon_T + \varepsilon_x. \quad (3)$$

Summarize:

$$\varepsilon = \varepsilon_e + \varepsilon^*. \quad (4)$$

The stress caused by elastic stress are:

$$\varepsilon_e = \varepsilon - \varepsilon^*. \quad (5)$$

The elastic stress can be obtained as:

$$\{\sigma\} = [D](\{\varepsilon\} - \{\varepsilon^*\}) \quad (6)$$

where  $[D]$  is the elastic matrix, it can be concluded that the elastic stress depends on the magnitude and distribution of the intrinsic strain  $\{\varepsilon^*\}$ .

Stress analysis is based on the temperature field of the melt and the changes in microstructure due to the temperature field. The temperature field can be determined either numerically or by experimental measurements, and the temperature changes in the material are usually accompanied by thermal deformation. If  $\alpha$  is the coefficient of linear expansion and the sufficiently small temperature change in the three coordinate directions is  $\Delta T$ , the volumetric thermal strain  $\varepsilon_T$  is:

$$\varepsilon_T = \alpha \Delta T. \quad (7)$$

**Table 2.** Parameters of the cube structure model.

	Cylindrical diameter (mm)	Cylindrical length (mm)	Unit aperture ( $\mu\text{m}$ )
Structural parameters	0.7	1.5	800

In SLM where  $\Delta T$  varies dramatically and the expansion coefficient  $\alpha$  is temperature dependent, the thermal strain, and corresponding variation induce elastic thermal and elastoplastic stress fields. Therefore the main focus in finite element analysis is on the evolution of the magnitude and distribution of residual stress through intrinsic strain inference.

In this study, the temperature and stress fields of the melt pool during the melting process were simulated using MSC Simufact Welding software. The cubic structure of the bone scaffolds model were meshed using hypermesh before the calculation, with a hexahedral mesh type and a size of 0.05 mm. The theoretical model was used for the analysis.

The sudden cooling and heating of SLM make the temperature field during processing can be seen as the temperature field when a transient point heat source acts on a semi-infinite body, and the SLM processing heat source is also usually seen as a Gaussian heat source processing. In this case, the heat propagates in three dimensions and the thermal propagation process of this point heat source within the semi-infinite can be described as:

$$dT(x, y, z, t) = \frac{2q(r)dx'dy'dt}{c\rho(4\pi at)^{3/2}} \exp\left(\frac{-R'^2}{4at}\right). \quad (8)$$

$$R'^2 = (x - x')^2 + (y - y')^2 + z^2, r^2 = x'^2 + y'^2, \quad (9)$$

where  $R'$  is the distance from any point  $A(x, y, z)$  in the powder bed to the instantaneous point heat source  $B(x', y', 0)$ ,  $c_p$  is the volumetric specific heat capacity of the material [ $\text{J}/(\text{mm}^3 \cdot ^\circ\text{C})$ ],  $a$  is the thermal diffusivity ( $\text{mm}^2/\text{s}$ ), and  $t$  is the heat transfer time (s).

$$q^*(r)dt = q_{\max}^* dt \exp(-kr^2), \quad (10)$$

where  $q^*$  is the heat flow density on the isothermal surface [ $\text{J}/(\text{mm}^2 \cdot \text{s})$ ] and  $k$  is the concentration factor of the Gaussian heat source. Taking equation (9) and equation (10) above into (8), calculated as:

*See equation (11) below.*

The whole Gaussian heat source is regarded as the sum of the countless micro source heat  $dQ$  added to the micro

element area. According to the superposition principle, the instantaneous point heat sources of each micro source are distributed on the whole area  $A$  in the  $xOy$  plane.

$$T - T_0 = \frac{2Q}{c\rho(4\pi at)^{3/2}} \exp\left(-\frac{r^2}{4at}\right), \quad (12)$$

$$T(r, z, t) = \int_A dt(x, y, z, t), \quad (13)$$

*See equation (14) below.*

In expressions, usually  $k = 1/(4at_0)$ ,  $q_{\max} = qk/\pi$ . The above formula is simplified to:

$$T(r, z, t) = \frac{2qdt}{c\rho} \left[ \frac{\exp[-z^2/(4at)] \exp\{-r^2/4a(t+t_0)\}}{(4\pi at)^{1/2} 4a(t+t_0)} \right]. \quad (15)$$

The second term in equation (15) above indicates the process of linear propagation of the heat of the virtual instantaneous plane heat source applied on the  $xOy$  plane parallel to the  $Oz$  axis inside the object, which starts when the application time is  $t = 0$ . The third term describes the plane radial propagation process of the virtual line heat source coincident with the  $Oz$  axis, which starts  $t_0$  time earlier than the time when the actual heat source is applied. The heat propagation process of an instantaneous Gaussian heat source in a semi infinite body can be regarded as the product of the linear heat propagation process expression and the plane radial heat propagation process expression.

## 2.5 Analysis and testing

For the study of the 316L porous bone scaffolds, samples were etching with aqua regia and analysis of the grain morphology size, etc. samples were carried out using a scanning electron microscope (SEM) (ZEISS SUPRA 55, Germany). Phase characterization of porous bone scaffolds using X-ray diffraction (XRD), (Rigaku smartlab, Japan). XRD measurements were made with a step size of  $0.05^\circ$  and a step time of 1 s across  $2\theta$  positions between  $20^\circ$  and  $100^\circ$ . Residual stress testing of porous bone scaffolds using X-ray diffraction (Proto, Lasalle, Canada). Corrosion resistance

$$dT(x, y, z, t) = \frac{2q(r)dx'dy'dt}{c\rho(4\pi at)^{3/2}} \exp\left(-\frac{(x-x')^2 + (y-y')^2 + z^2}{4at} - k(x'^2 + y'^2)\right). \quad (11)$$

$$T(r, z, t) = \frac{2q_{\max}dt}{c\rho(4\pi at)^{3/2}} \int_{-\infty}^{+\infty} \int_{-\infty}^{+\infty} dx'dy' \exp\left[\frac{(x-x')^2 + (y-y')^2 + z^2}{4at} - \frac{(x'^2 + y'^2)}{4at_0}\right]. \quad (14)$$

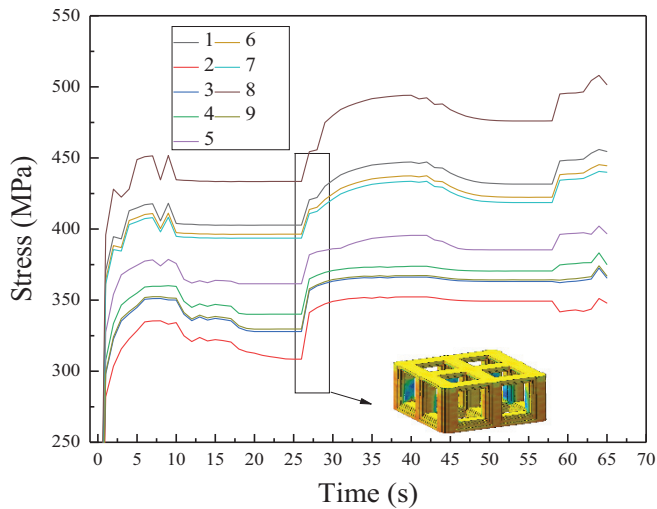


**Fig. 3.** Stress changes during the construction of porous bone scaffolds for column structure.

testing of samples using electrochemical workstations (CHI760E, China).

### 3 Results and discussion

In this study, the effect of energy density on residual stress in the scaffold is used as an entry point to investigate the link between residual stress and defects such as holes and cracks, and to investigate the residual stress and the histomorphology of the scaffold for different build energy densities to select the appropriate build parameters to improve the quality of forming.

#### 3.1 Residual stress

According to the theory of inherent strain, different construction process parameters result in different values of inherent strain, which is mainly present in and around the welds of the scaffolds, and the magnitude and distribution of the inherent strain determines the final residual stress and deformations [28–31].

Figure 3 shows the variation of the instantaneous residual stress during the construction of the scaffold for different construction process parameters. It can be seen from the figure that for the cubic structure of the porous bone scaffolds the build instantaneous residual stress and the post-build residual stress are both minimal at an energy density of  $41.7 \text{ J/mm}^3$ , in contrast to the 8# test scenario where the build and post-build stress were consistently highest at an energy density of  $111.1 \text{ J/mm}^3$ . The residual stress in the construction are most pronounced on the upper surface of the substrate where the cladding was applied, while forces were generated inside the porous scaffolds due to force interactions against the residual stress in the substrate, as the build height increases, the uneven repetitive thermal cycling causes frequent thermal expansion and contraction within the substrate, which introduces a large amount of residual stress, which in turn

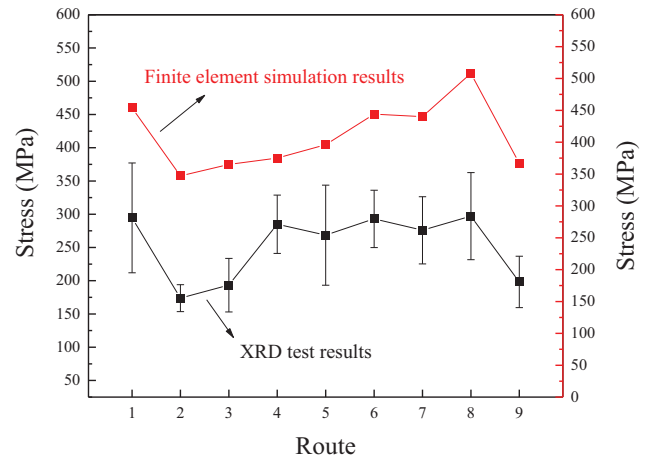


**Fig. 4.** Residual stress test results.

affects the magnitude of the stress on the scaffolds. It can be seen from the figure that when it is built to about 50%, the residual stress inside the scaffolds also increases suddenly (as shown by the black box in the figure). It is speculated that the reason is that the cross column part starts to be built at this time, and the increase of the solidification layer area makes the solidification contraction stage subject to the resistance of the connection part with the column against contraction in addition to the internal stress generated by itself. With the continuous addition of new layers, the deformation is constantly hindered, a new internal stress is introduced, and the compressive stress is introduced in the corresponding solidified layer, which increases cumulatively.

For the test of residual stress, the XRD method is selected in this study. XRD diffraction testing of residual stress is based on the change in the face spacing of specific grain faces within the grain when elastic stress is applied to the grains that make up the material, and thus the residual stress are calculated. The test results and finite element simulation results are shown in Figure 4. It can be seen from the Figure 4, that there is a large error range in the actually measured residual stress value because the X-ray can only pass through the material surface  $30 \mu\text{m}$ , in order to better study the impact of test parameters on the forming quality of the porous scaffolds, the surface of the porous scaffolds were not polished before the test, resulting in a large roughness affecting the error range of the test. In the XRD test results, it was found that the surface of the porous scaffolds were all compressive stress. The porous scaffolds formed by the 2# test scheme had the smallest residual stress, and the 8# test scheme had the largest residual stress.

The analysis of the residual stress test results showed that the residual stress formed when using low energy density ( $\leq 57.1 \text{ J/mm}^3$ ) were more desirable, and the residual stress obtained with the 2# and 9# experimental solutions were always at the minimum, after summarising the factors that determine the energy density, it was found that the powder thickness and hatching spacing used for 2# and 9# test schemes were the same, while the laser power and scanning speed differed significantly. Then, in

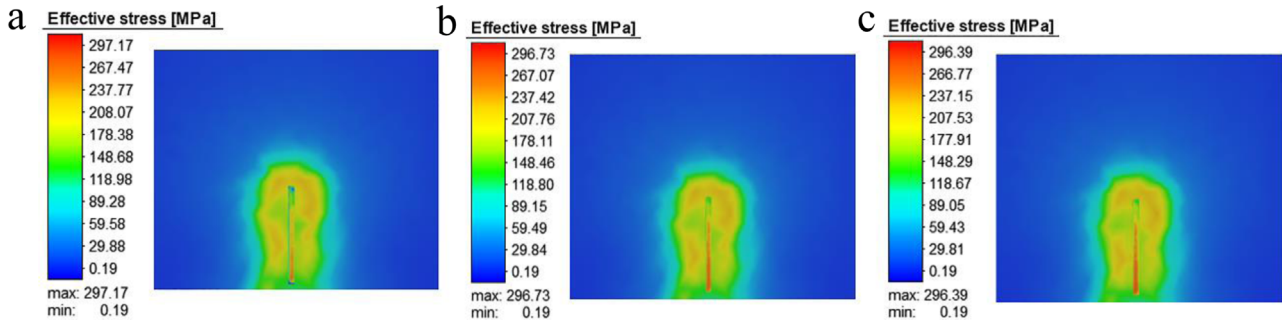


Fig. 5. Effect of hatching spacing on residual stress: (a)  $s = 0.06$  mm, (b)  $s = 0.08$  mm, (c)  $s = 0.10$ .

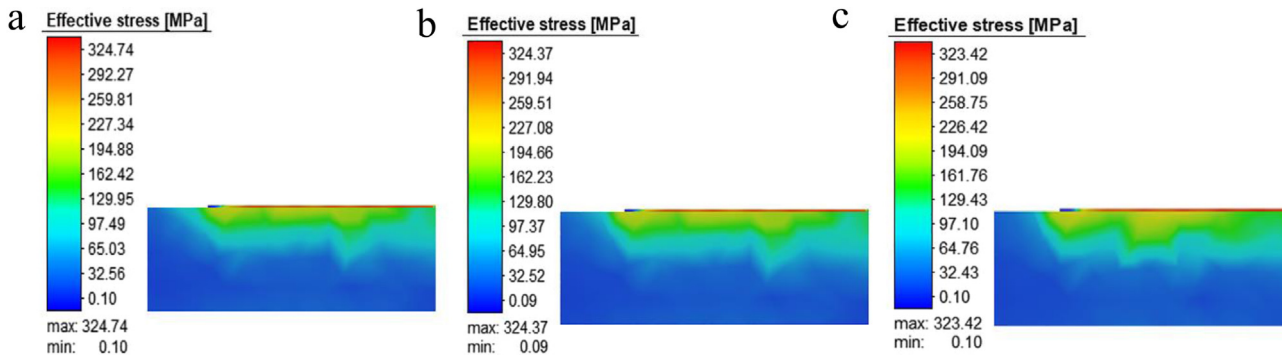


Fig. 6. Effect of laying powder thickness on residual stress: (a)  $t = 0.03$  mm, (b)  $t = 0.04$  mm, (c)  $t = 0.05$  mm.

order to verify whether the magnitude of the residual stress is related to the hatching spacing and powder thickness, we did finite element analysis calculations based on the 2# test scheme construction plan and changed the hatching spacing and powder thickness, the results are shown in Figures 5 and 6. It can be seen from the results that there is almost no difference in the residual stress obtained by changing the hatching spacing, but the residual stress of the thickness with  $t = 0.05$  is reduced by about 0.4% compared with other thicknesses in the powder coating thickness. The slight change brought by the change of the powder coating thickness makes us make a bold guess. In SLM processing, the effect of the hatching spacing and the powder coating thickness on the residual stress exists but is small, which can be seen as having almost no effect. Then we looked up other relevant literature and found that our result was basically consistent with the research conclusions of other scholars [32].

The presence of residual stress in porous scaffolds was caused by the inhomogeneous temperature sites created during the laser melting process, where the temperature within the melt pool can reach up to the boiling point of the materials during laser melting and then drop sharply after the heat source has left. From equation (14) we see that the temperature field of the melt pool is mainly related to the volume-specific heat capacity of the materials, processing time, and thermal diffusivity, while the specific heat capacity and thermal diffusivity are the nature of the materials under certain conditions, the conditions change, they will also change, for example the specific heat capacity and thermal diffusivity of substances at different

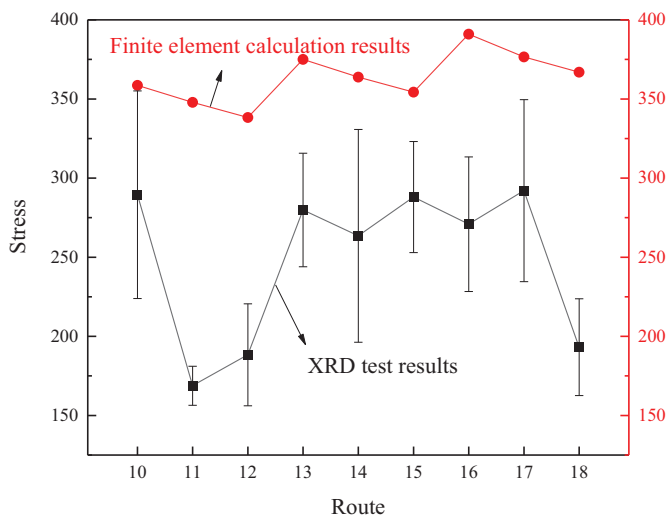
temperatures are different. When the thickness of the powder layer is changed, the laser absorption rate in the old layer is likely to change, which in turn changes the temperature, leading to changes in specific heat capacity and thermal diffusivity. However, the finite element analysis found that the change in layer thickness had a small effect on the temperature field, presumably due to the small change in layer thickness (0.02 mm difference in layer thickness) and the minimal difference in laser absorption. In addition, it was found that the higher melt pool temperature apparently allows for better bonding of the clad layer, but also leads to the introduction of a large amount of thermal stress, which causes the solidified layer and the substrate to generate corresponding internal stress during cooling, thus increasing the residual stress.

At the same time, in order to more comprehensively explore the impact of laser power and scanning speed on bone scaffolds in the construction parameters, the study decided to arrange and combine the construction parameters more accurately according to the results in the previous text, in order to better explore the impact of construction parameters on performance. The specific experimental scheme is shown in Table 3.

Figure 7 shows the residual stress test results for process options 10#–18# experimental programmes. The study combined with the test results in Figure 4 suggests that the residual stress introduced by the lower energy density used in the construction of the porous bone scaffold of the cubic structure are also relatively low. In addition, the pattern of results from the finite element simulations is generally consistent with the experimental test results as seen in

**Table 3.** Experimental programme on laser power and scanning speed.

Experimental programme	Laser power $P$ (W)	Scanning speed $V$ (mm/s)	hatching spacing $S$ (mm)	Energy density $E$ (J/mm <sup>3</sup> )
10#	100	500	0.10	50.0
11#	100	600	0.10	41.7
12#	100	700	0.10	35.7
13#	130	500	0.10	65.0
14#	130	600	0.10	54.2
15#	130	700	0.10	46.4
16#	160	500	0.10	80.0
17#	160	600	0.10	66.7
18#	160	700	0.10	57.1

**Fig. 7.** Residual stress test results.

Figures 4 and 7, demonstrating that the pattern of influence of the finite element simulation construction parameters on the stress in the porous scaffolds can provide a degree of reference for the actual test.

Figure 8 shows the distribution of the residual stress in the construction of different structures. From Figure 8, it is found that the higher stress in the scaffolds are found on the edge of the unit column, probably due to the restriction of the solidified layer below and the unmelted powder nearby during the cooling and shrinking phase, which prevents the melt pool from shrinking freely and leads to uneven plastic deformation at the edge of the scaffolds and introduces residual stress. In addition, the thermal conductivity of the solidified area is significantly higher than that of the surrounding powder, resulting in an early cooling of the middle part and a larger temperature gradient with the edges, thus creating residual stress at the edges.

It can also be seen in Figure 8 that after the scaffold is cut from the substrate, the residual stress at the bottom is significantly reduced, and the distribution range of the residual stress is significantly reduced. It is speculated that the reason is that when fewer layers are built, the larger temperature gradient makes the base plate and the bottom

of the scaffold generate mutually resistant internal stress. When the scaffold is cut from the base plate, the bottom of the scaffold becomes unconstrained, and the residual stress is released, thus reducing the internal residual stress.

### 3.2 Residual deformation

The main causes of process defects such as deformation and cracking in scaffolds were caused by residual stresses introduced during the construction process. Porous scaffolds are known as the ideal material for bone replacement due to their excellent structural customizability, but the presence of residual stress can easily produce different degrees of deformation, which can jeopardize shape and dimensional tolerances and lead to functional failure of the scaffold. As a result of the above study, it was found that the use of different process parameters in the SLM forming process of porous scaffold structures is likely to have different degrees of influence on the residual stress in the scaffold, which are generated by strain, and therefore investigating the influence of different process parameters on the amount of scaffold deformation is necessary to improve the forming accuracy. Figure 9 shows the comparison of the deformation of the porous bone scaffolds in the finite element simulation of the column structure, it can be seen that the deformation of the formed scaffolds under the 9 process parameters has a large difference, among which the largest deformation is the bone scaffold formed by the 8# test scheme, the maximum deformation of the cubic structure reaches 0.75%, on the contrary, the bone scaffold formed by the 2# test scheme produces a smaller deformation.

Figure 10 is a comparison diagram of the finite element analysis results and the test results of the deformation of the porous scaffolds. As can be seen from Figure 10a, the deformation of the cube structure is concentrated on the lower surface of the cross column of the unit. The reason why the deformation occurs at this position can be seen in Figure 11. The horizontal column structure is in a suspended state, and 316L metal powder acts as a support. After the first laser irradiation, a large amount of powder rapidly flows into the molten pool, forming an obvious slump at the irradiation site, and there are different degrees of powder adhesion around the solidified layer. When the laser is irradiated again, the powder on the upper surface of

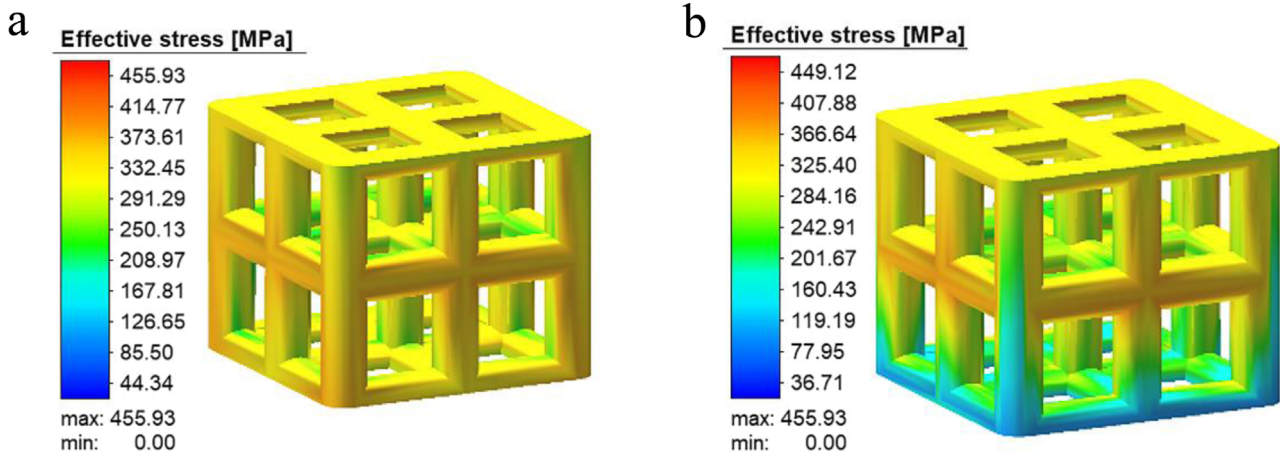


**Fig. 8.** Residual stress distribution in the porous scaffold of the column structure: (a) Before removal of the conventional cubic structure substrate, (b) After removal of the conventional cubic structure substrate.

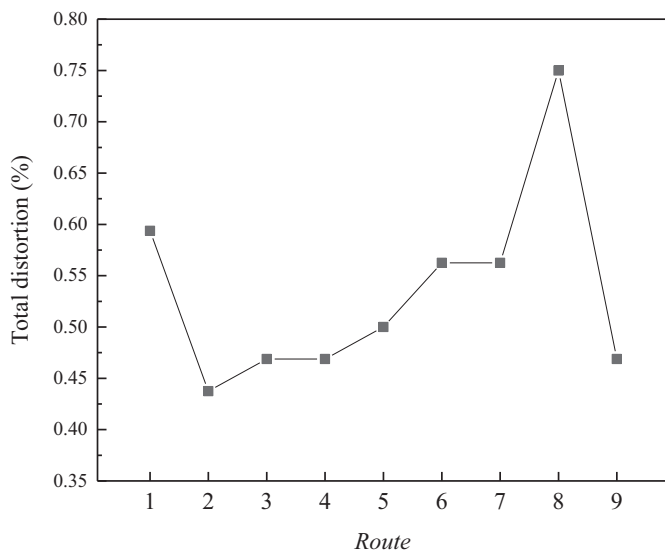


**Fig. 9.** Comparison of deformation of porous bone scaffolds.

the solidified layer is melted under the action of the high-energy laser beam, and the unmelted powder brought by the adhesion of the surface inclusions or the blowing inside the powder bed is also remelted. This process is repeated, thus reducing upper surface adhesion and balling. On the contrary, due to the characteristics of additive forming, there is no direct irradiation of the laser beam below the solidified layer, but the constant heat transfer causes repeated thermal expansion and contraction of the solidified layer, which is very easy to attract powder adsorption and form a large number of deposits. We can also observe from Figure 10b that most of the suspended powder on the lower surface of the cross-column structure is loosely attached, and the residue on the upper surface is tightly fused with the column. The accumulation and stacking of a large number of powders not only affects the forming accuracy of bone scaffolds but also affects the surface roughness to a large extent. Moreover, the

accumulation of a large number of powders is easy to produce a small amount of stress concentration at the stacking position.

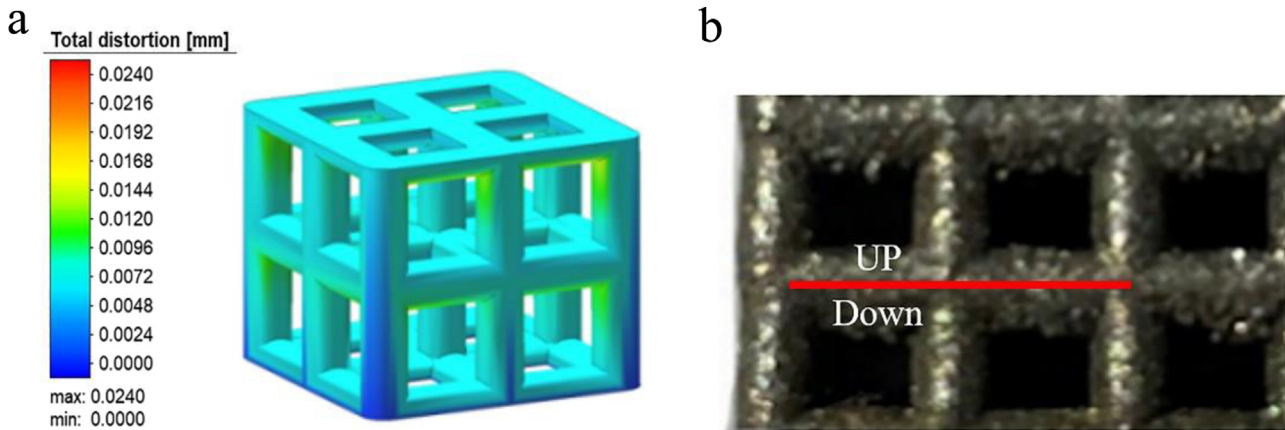
### 3.3 Microstructure

Figure 12 shows the microstructure of the cubic structure at different process parameters, with typical and uniform defects selected for analysis with a build energy density between  $35.7 \text{ J/mm}^3$  and  $111.1 \text{ J/mm}^3$ .

It can be seen from the figure that there are significant differences in the forming quality of the scaffolds under different process parameters. Although the scaffolds can be formed macroscopically when the porous bone scaffolds are constructed with energy density  $< 41.7 \text{ J/mm}^3$  as shown in Figure 12a, there are a large number of irregular holes in the internal microstructure, and a large number of residues left over from the forming process have adhered to the surface. It can be seen from the figure that a large number of unmelted powder particles are mixed in the holes and causing great difficulty in etching. As can be seen from the other diagrams, the defects are mainly divided into two main categories, one is the macroscopic range of relatively large holes, this kind of hole through the length accompanied by the generation of cracks, and the other is distributed on the edge of the melt pool, this kind of more presents the characteristics of a large number of small diameter. In order to better investigate the changes in the temperature and stress fields of the melt pool during SLM forming, finite element simulations of the melt pool with different energy densities were carried out in this study. The results are shown in Figures 13 and 14.

Figures 13 and 14 show the changes in the temperature field and the stress field of the SLM construction pool under different energy densities.

As can be seen from the results in Figure 13 based on finite element simulations, the intuitive effect brought about when the energy density is significantly increased is a sharp increase in temperature within the melt pool, the most obvious of which is the change in temperature at the



**Fig. 10.** Distribution of deformation in porous bone scaffolds: (a) Finite element simulation of the situation, (b) SLM formed of the situation.

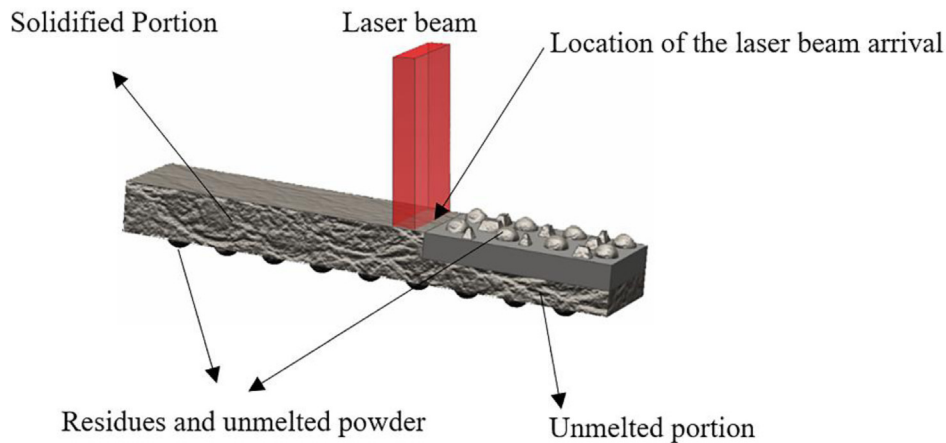


**Fig. 11.** Schematic representation of the principle of additive manufacturing.

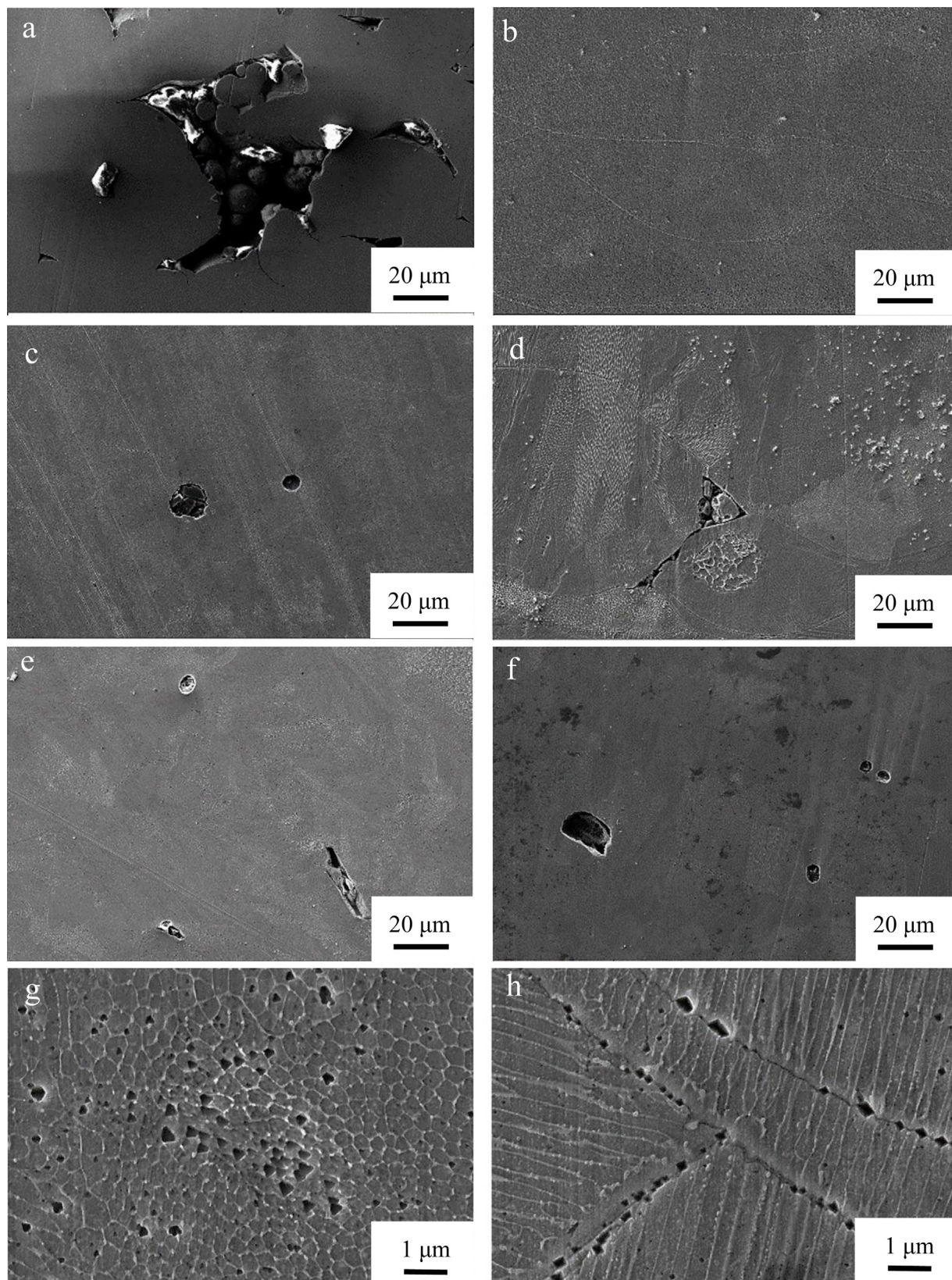
spot focus position and comet tail during laser processing. The whole process of SLM can be seen as a temperature field under a continuously moving concentrated heat source, and due to the different processing parameters, the temperature field will have a large impact. SLM processing is characterized by a faster-moving heat source and a more complex temperature field distribution during processing. Generally, engineering will simplify it before establishing a mathematical model to qualitatively analyze the temperature field. In the processing process, the laser heat source to speed  $v$  to do uniform linear motion, the thermal power in the direction of the powder bed powder thickness is  $q/h$ , from the moving heat source  $r$  at the temperature  $T$  is:

$$T(x, y, z) = \frac{q}{4\pi\lambda h} \exp\left(-\frac{vx}{2a} \int_0^t \frac{dt''}{t''}\right) \exp\left[-\left(\frac{v^2}{4a} + b\right)t'' - \frac{r^2}{4at''}\right], \quad (16)$$

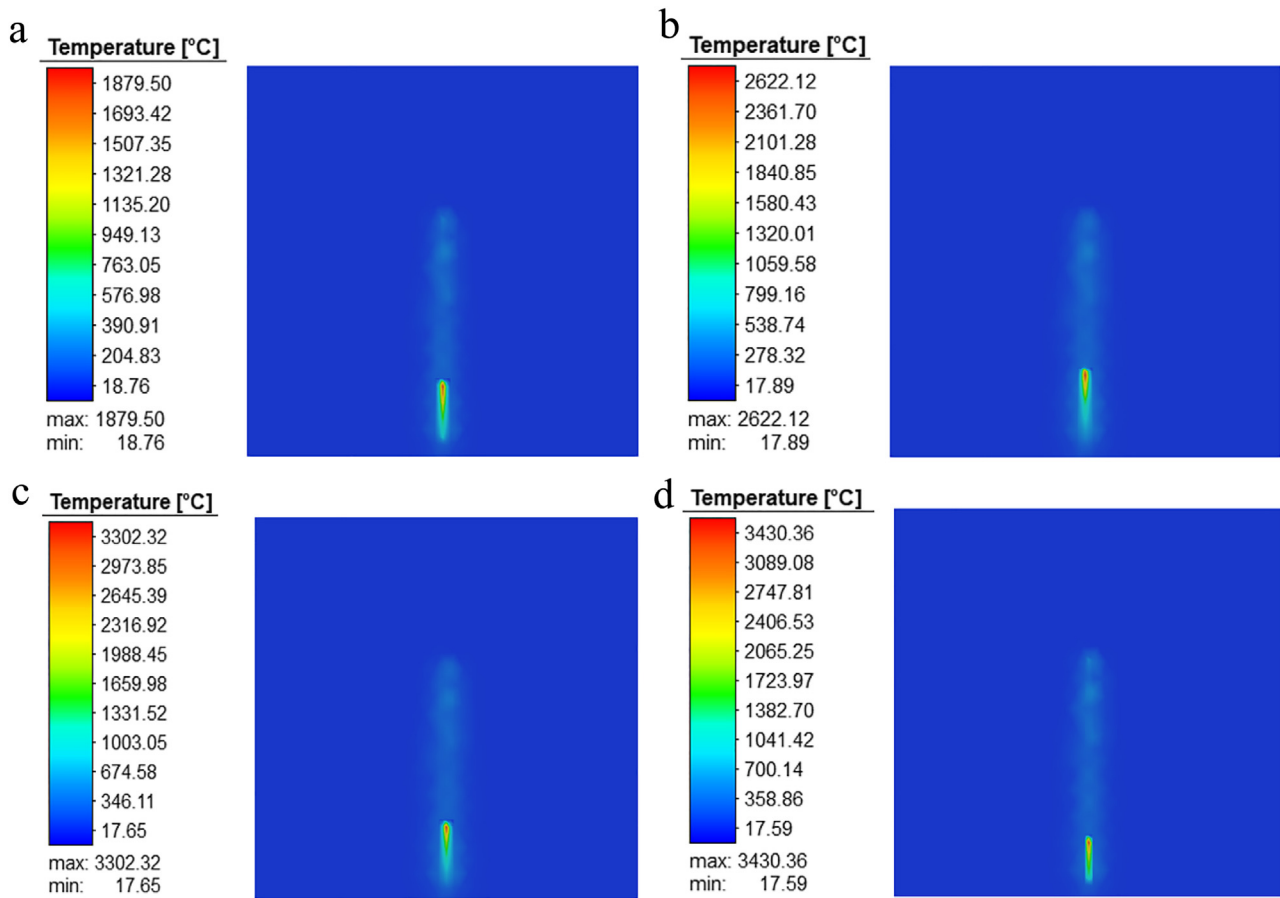
in the formula,  $r^2 = x^2 + y^2$ ,  $\lambda$  is the thermal conductivity [J/(mm · s · K)],  $a$  is the thermal diffusivity (mm<sup>2</sup>/s),  $t$  is the heat transfer time (s),  $b$  is the temperature dispersion coefficient (s<sup>-1</sup>),  $q$  is the effective thermal power (J/s).

Figure 14 shows the change in the stress field of the melt pool during the construction process at different energy densities. The initial temperature in the centre of the melt pool is the highest during the SLM process, but the internal thermal stress is not the greatest at this time, as can be seen from Figure 14. This is because the thermal stress at this point should be the sum of the thermal stress at the start of cooling with the addition of the thermal stress of the machining process, and the magnitude and distribution of the residual stress were also determined by the thermal stress during heating and cooling and the plastic deformation they caused. The simulated calculation of the stress field in Figure 14 shows that the energy density is proportional to the magnitude and distribution of the stress field.

Figure 15 shows the tissue grain inside the scaffolds at different energy densities. Combining Figure 15 and Figure 14a we interpret a large number of holes in Figure 12a as a result of the lower temperature field at an energy density of 35.5 J/mm<sup>3</sup>, thus causing less thermal stress and thus less residual stress. However, it is found from Figure 12a that after the laser scanning, the low energy density makes the metal powder not completely



**Fig. 12.** Microstructure of the scaffold at different energy densities: (a)  $E=35.5\text{ J/mm}^3$ , (b)  $E=41.7\text{ J/mm}^3$ , (c)  $E=54.2\text{ J/mm}^3$ , (d)  $E=65.0\text{ J/mm}^3$ , (e)  $E=77.4\text{ J/mm}^3$ , (f)  $E=80.0\text{ J/mm}^3$ , (g)  $E=100.0\text{ J/mm}^3$ , (h)  $E=111.1\text{ J/mm}^3$ .



**Fig. 13.** Variation of the melt pool temperature field during construction at different energy densities: (a)  $E = 35.5 \text{ J/mm}^3$ , (b)  $E = 65.0 \text{ J/mm}^3$ , (c)  $E = 80.0 \text{ J/mm}^3$ , (d)  $E = 111.1 \text{ J/mm}^3$ .

melted, resulting in a large amount of unmelted powder and residual molten pool remaining in the weld bead during the solidification process, which makes the molten pool unable to solidify normally. Macroscopically, it shows a hole phenomenon. When the temperature drops and the molten pool is completely solidified, the remaining holes are affected by the resistance to contraction of the substrate and the solidified part, thereby generating cracks. After repeated laser irradiation and heating, the solidified part expands under the action of thermal stress, causing cracks to increase and large cavities to be formed. In addition, powder bed processing is characterized by good powder fluidity, which is especially easy to fill into the holes. After repeated irradiation, many holes with powder are formed, resulting in a sudden decline in forming quality.

For some other holes remaining on the scaffolds, as shown in (c)–(f) in Figure 12, our analysis shows that there are two main reasons for the formation. One is improper processing parameters, such as the selection of a lower scanning speed under high laser power, which makes the laser beam stay too long in the processing process and causes overheating. The interior of the molten pool becomes extremely active, providing conditions for the influx of powder. For the solidified layer, continuous high-power laser irradiation may cause remelting, which

enlarges the original micro-crack defects. It is worth noting that overheating can also introduce a large amount of residual stress, which corresponds to the sudden increase of stress in Figures 14b–14d compared with Figure 14a, or the low laser power selects a higher scanning speed so that the dwell time of the laser beam in the processing process is too short and the energy generated is not enough to form a hole generation mechanism similar to that in Figure 12a. The other is due to gas, where the forming bin is filled with protective gas and the protective gas does not escape in time to be enclosed in the molten metal fluid after a fast laser scan to form a round hole, or where the energy density is too high causing a small amount of metal fluid to vaporize and form a hole. For the relatively small holes as in Figures 12e and 12f, it is speculated that the reason for this is that the larger construction area of the cross pillar during the construction of the cubic structure allows the influence of the laser beam heat source to increase, and the thermal deformation of the material in the high-temperature zone adjacent to the melt pool is limited by the surrounding material, which tends to produce uneven compressive plastic deformation, especially the uneven subcooling near the edge of the melt pool leading to more defects due to the inability to form nuclei or the destruction of the grain growth process.

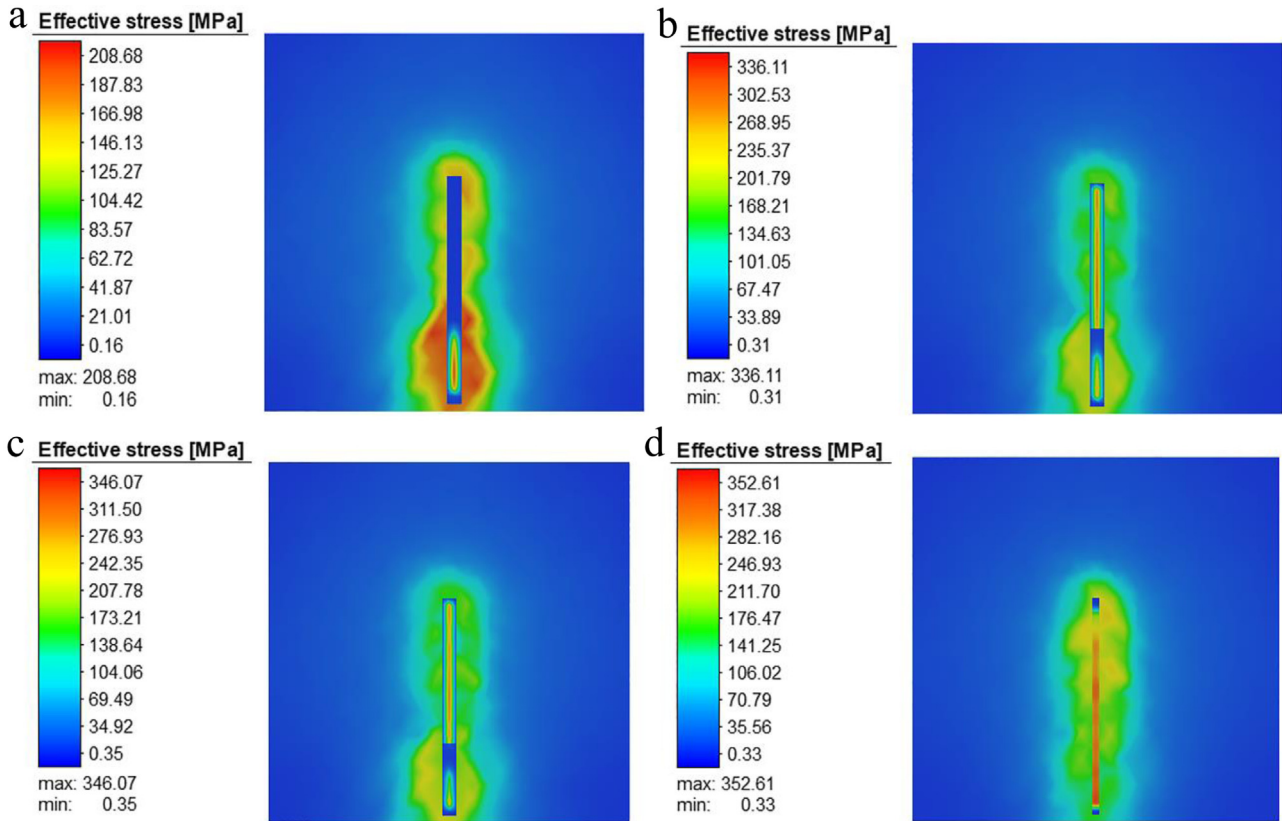


**Fig. 14.** Variation of the melt pool stress field during construction at different energy densities: (a)  $E = 35.5 \text{ J/mm}^3$ , (b)  $E = 65.0 \text{ J/mm}^3$ , (c)  $E = 80.0 \text{ J/mm}^3$ , (d)  $E = 111.1 \text{ J/mm}^3$ .

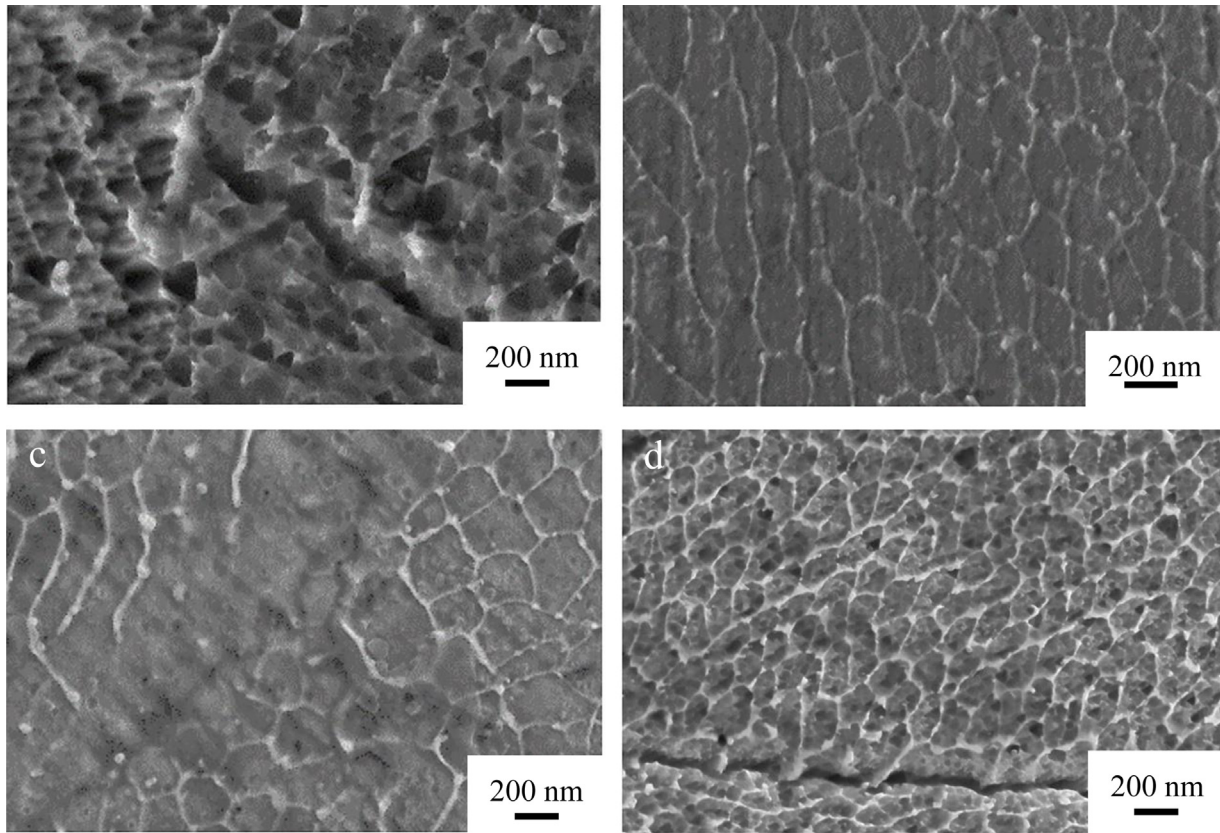
In addition, during solidification, the low surface tension area at the edge of the molten pool was easily pulled to the high surface tension area, resulting in the deformation of the grains in the molten pool. As can be seen more directly from Figure 15, the grains under high-energy processing show multiple patterns. There are long equiaxed grains or deformed equiaxed hexagonal grains near the edge of the molten pool, and it is observed that the long grains are not perpendicular to the tangent of the edge of the molten pool. It is at an angle of  $<90^\circ$  with the tangent line. The reason for this is that the thermal stress inside the molten pool affects the grain growth direction, and the preferred orientation growth of grains is also a factor to consider. The existence of a large number of deformed grains, coupled with the continuous effect of the upper laser thermal cycle, is prone to produce defects near the edge of the weld pool, while the inside of the weld pool is dominated by equiaxed hexagonal grains, which are closely arranged and regular, with fewer defects.

Table 4 shows the grain size under various process routes. Different construction methods with different energy densities will form different temperature fields, thus resulting in different nucleation rates. From Table 4, we can see that the energy density and grain size do not show a specific relationship, but through analysis, we find that there is a law, that is when lower laser power is used, if lower scanning speed is also selected (such as the processing parameter of  $E = 83.3 \text{ J/mm}^3$ ), the grain formed is

relatively small, which can reach 420 nm. In addition, if a higher laser power is used, a higher scanning speed (such as the processing parameter of  $E = 57.1 \text{ J/mm}^3$ ) should be used to form a relatively ideal grain size. For the case of large grain size, it is speculated that the reason may be that repeated high-energy beam irradiation causes the solidified layer to absorb a large amount of heat to promote grain growth and deformation.

The  $2\theta$  ( $20^\circ$ – $100^\circ$ ) XRD spectra of the porous bone scaffolds at different energy densities are shown in Figure 16, from which it is seen that only the FCC austenite phase is present inside the SLM-formed 316 L porous bone scaffolds and no other phases are produced. For the  $2\theta$  position, diffraction peak intensity, half-peak width of the main peak, and other data are shown in Table 5. The test results show that the data from XRD at different energy densities vary considerably. A comparison with the standard  $\gamma$ -Fe phase  $2\theta$  position shows that the porous scaffolds formed by SLM processing has a slight shift in the  $2\theta$  position, which is due to residual stress and associated lattice distortion caused by the SLM process. In addition, the build direction chosen for the construction was  $90^\circ$  build, so (220) was used as the preferred orientation of the planes and the peak height of the (220) planes was found to increase with increasing energy density by varying the energy density.

SLM forming of porous scaffolds tends to affect the surface roughness due to the forming characteristics, which



**Fig. 15.** SEM image of scaffold tissue grains: (a)  $E = 83.3 \text{ J/mm}^3$ , (b)  $E = 41.7 \text{ J/mm}^3$ , (c)  $E = 100.0 \text{ J/mm}^3$ , (d)  $E = 111.1 \text{ J/mm}^3$ .

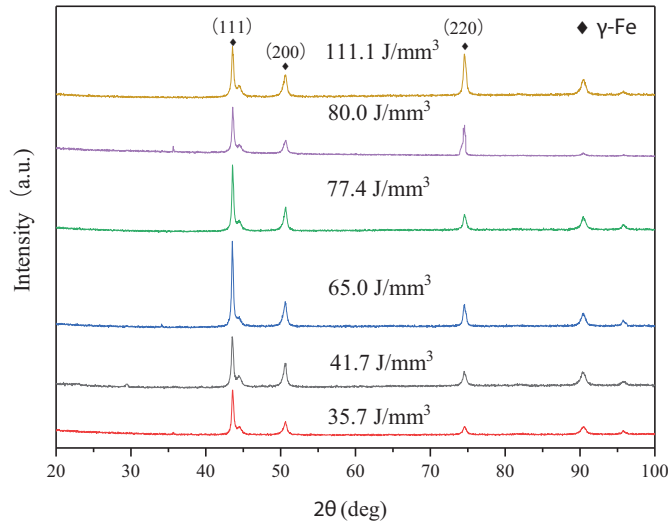
**Table 4.** Grain size at different energy densities.

Energy densities ( $\text{J/mm}^3$ )	35.7	41.7	44.6	46.4	50	54.2	57.1	65	66.7	77.4	80	83.3	100.0	111.1
Grain size (nm)	508	441	481	427	477	454	429	490	501	446	525	420	540	546

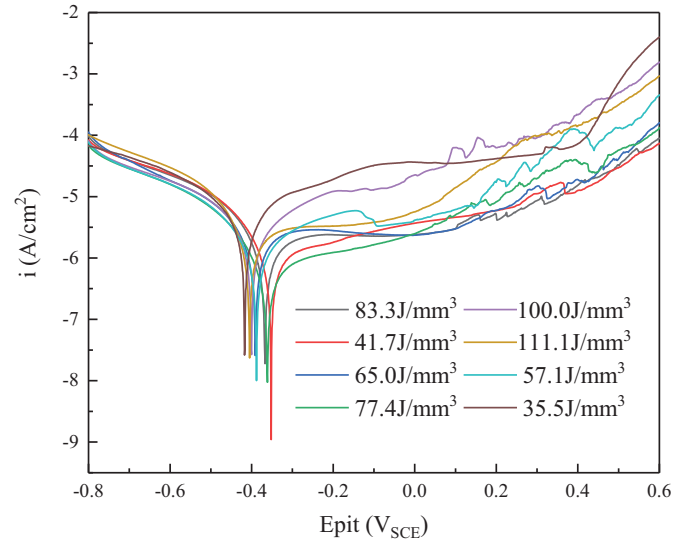
in turn affects the forming accuracy, making the actual hole size constructed smaller than the theoretical design model. As a result of the above study on residual deformation, it is concluded that the selection of a suitable energy density during the construction can maximize the control of the forming accuracy of the scaffold and reduce the residue build-up and spherification phenomenon.

Figure 17 shows the electrochemical corrosion of the porous bone scaffolds at different energy densities. From the figure, we can see that the corrosion potential is at a larger value when using an energy density of  $41.7 \text{ J/mm}^3$  and that there is some variation in the corrosion current, which is not always at a minimum as expected. In addition, combined with the content of grain size under different energy densities mentioned above, it is introduced that the grain size obtained at the energy density of  $83.3 \text{ J/mm}^3$  is the smallest, followed by  $41.7 \text{ J/mm}^3$ , and the maximum size reached 540 nm and 546 nm at the energy density of  $111.1 \text{ J/mm}^3$  and  $100.0 \text{ J/mm}^3$ , respectively.

Interestingly, the worst corrosion resistance was achieved at an energy density of  $35.5 \text{ J/mm}^3$ , but its grain size was not the smallest. Combined with the microstructural differences mentioned above, it is assumed that the reason for this is a large number of holes and cracks created on the surface of the porous bone scaffolds during construction using this energy density, as well as the unfused powder providing favorable conditions for localized pitting corrosion. Additionally, according to the electrochemical corrosion results shown in Figure 17, the corrosion resistance of the scaffolds obtained with energy densities of  $41.7 \text{ J/mm}^3$  and  $83.3 \text{ J/mm}^3$  was superior to other processing parameters. It is speculated that the finer grain structure may help form a denser passive oxide layer when SLM is used to form 316L porous bone scaffolds, thus resulting in better corrosion resistance. The results of the electrochemical corrosion rate obtained in this study are basically consistent with the theory proposed by Ralston et al. [33] that with the decrease of grain size, the corrosion rate decreases (that is, the corrosion resistance improves).



**Fig. 16.** XRD pattern of the stainless steel parts processed by SLM under different  $E$ .



**Fig. 17.** Typical cyclic dynamic potential polarisation curve of porous bone scaffolds.

**Table 5.** XRD data showing the  $2\theta$  values, intensity and peak FWHM of the main peaks.

Sample	$2\theta$ location	Intensity	Peak FWHM
Standard (PDF NO.33-0937)	43.582	/	/
35.5 J/mm <sup>3</sup>	43.520	1643	0.476
41.7 J/mm <sup>3</sup>	43.520	1891	0.412
65.0 J/mm <sup>3</sup>	43.565	3080	0.343
77.4 J/mm <sup>3</sup>	43.566	2393	0.323
80.0 J/mm <sup>3</sup>	43.565	1987	0.414
111.1 J/mm <sup>3</sup>	43.565	1895	0.459

It has been reported [33–35] that 316L stainless steel products manufactured with SLM are superior to conventionally forged 316L stainless steel in terms of corrosion resistance and physical compatibility, and current research into the corrosion resistance of austenitic stainless steel continues to focus on the role of MnS inclusions and their role in corrosion. It has been found that low concentrations of Cr in 316L can easily lead to significant pitting in stainless steel, and the presence of small defects, often combined with the highly corrosive nature of human body fluids, is likely to cause significant degradation in the performance of scaffolds, and all aspects of the performance of bone scaffolds used as functional implants must be studied and optimized. Through our analysis of the XRD pattern of the porous bone scaffold in the previous text, we found that the content of Ni and Cr in the formed part was high, only a single austenite phase was obtained, and the content of MnS was not high. This is what we expected, and we believe that this is also a reason why the SLM formed part has excellent corrosion performance. As for the reason for the low content of MnS, we speculate that the inherent rapid solidification rate of SLM technology leads to the reduction of the density and size of MnS inclusions. The

study also investigated the relationship between residual stress and corrosion resistance and found that the worst corrosion resistance was found for scaffolds formed at 35.5 J/mm<sup>3</sup>, followed by scaffolds formed at 111.1 J/mm<sup>3</sup>, which clearly differs from other authors' [36,37] findings that residual stress can positively affect the corrosion resistance of workpieces. The findings of this paper are that larger surface residual stress do not improve the corrosion resistance of the scaffolds. The studies on residual stress and corrosion resistance are still ongoing, but for this study, the reason for the discrepancy with others is that we speculate that there are more defects such as holes on the surface of porous scaffolds with higher residual stress (e.g. scaffolds formed using 35.5 J/mm<sup>3</sup> and 111.1 J/mm<sup>3</sup>), and this causes a reduction in corrosion resistance. However, the deeper mechanism of influence is beyond the scope of this paper, all we know so far is that SLM formed parts have good or even better corrosion resistance than ordinary means of forming 316L stainless steel products.

However, whatever the reason, what we know is that SLM-shaped parts have good or even better performance than 316L stainless steel products formed by ordinary means.

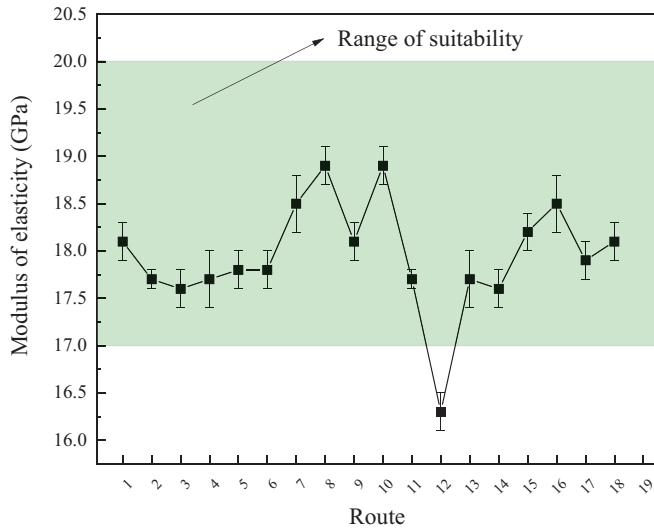


Fig. 18. Modulus of elasticity of porous bone scaffolds.

### 3.4 Modulus of elasticity of the bone scaffold

In order to better adapt to the mechanical properties of human bone, the modulus of elasticity of the porous bone scaffolds becomes the primary prerequisite for measuring whether the porous bone scaffold meets the implantation requirements, and the Gibson-Ashby formula [38] is usually used as the guiding model for calculating the modulus of elasticity of porous parts. shown below.

$$\frac{E^*}{E_s} = C \left( \frac{\rho^*}{\rho_s} \right)^m, \quad (17)$$

where  $E^*$  is the elastic modulus of the porous bone scaffold,  $E_s$  is the elastic modulus of its solid,  $E_s = 210$  GPa,  $\rho^*$  is the density of the porous bone scaffold,  $\rho_s$  the density of its solid,  $\rho_s = 7.98$  g/cm<sup>3</sup>,  $C$  and  $m$  are the geometric constants of the open structure  $C = 1$  and  $m = 2$  respectively. After cleaning the porous bone scaffold, the actual elastic modulus of the porous bone scaffolds was measured as shown in Figure 18. The elastic modulus of human cortical bone is 17–20 GPa, and that of cancellous bone is 3.2–7.8 GPa. The green area in the figure is the applicable range of human bone implants. From the figure, it can be seen that most bone scaffolds meet the requirements of implants, and only the 12# processing route has deviation. It is speculated that the reason is that the density of scaffolds has changed significantly due to the quality of scaffolds is lighter than other scaffolds, so the existence of surface holes.

Through the above research, it is shown that when SLM is used to form the porous bone scaffolds with a cubic structure, most of the processing parameters can meet the requirements of human bone elastic modulus and can be used as a cortical bone implant scaffolds. In addition, with appropriate processing parameters, the shaped scaffolds can have the function of long-term service with low forming defects.

## 4 Conclusion

- The magnitude of residual stress in SLM construction increases as the energy density increases, showing a positive relationship between the two. However, the construction of 35.7 J/mm<sup>3</sup> results in lower residual stress but poorer microstructure, while 41.7 J/mm<sup>3</sup> results in better microstructure and can therefore be used for the construction of porous bone scaffolds with cubic structure.
- The difference in energy density results in a change in grain size, which leads to a difference in the corrosion resistance of the scaffolds, which is significantly reduced at energy densities  $\geq 83.3$  J/mm<sup>3</sup> or less than 35.7 J/mm<sup>3</sup>, while the scaffolds show excellent corrosion resistance at other energy densities.
- The combination of low laser power with low scanning speed or high laser power with high scanning speed can be used for the construction of porous bone scaffolds with the cubic structure to obtain small residual stress and more desirable organization and properties, and the effect of hatching spacing on the temperature and stress fields of the melt pool is small and can be ignored.
- The use of finite element analysis as a means of prediction and optimization in the construction of porous bone scaffolds by SLM can provide theoretical guidance for defects, etc. in the scaffolds.

## Conflict of interest

Authors declare no conflict of interest.

## Author's contribution

Sen Zhang: Data curation, Formal analysis, Writing Original draft preparation, Software.

Shubo Xu: Conceptualization, Methodology, Review & Editing, Funding acquisition.

Wei Zheng: Investigation, Methodology, Resources.

Juanjuan Han: Funding acquisition, Resources, Supervision, Review & Editing.

This study was supported by Natural Science Foundation of Shandong Province (ZR2021ME182); State Key Laboratory of Material Forming and Mould Technology Open Fund Project (P12); National Natural Science Foundation of China (52105377).

## References

1. A. Naghmeh, H. Stephen, M. Love Robert et al., Porous scaffolds for bone regeneration, *J. Sci.: Adv. Mater. Dev.* **5**, 1–9 (2020)
2. X.W. Shanqing Xu, S. Zhou, Topological design and additive manufacturing of porous metals for bone scaffolds and orthopaedic implants: a review, *Biomaterials* **83**, 127–41 (2016)
3. S. Barui, S. Chatterjee, S. Mandal et al., Microstructure and compression properties of 3D powder printed Ti-6Al-4V

- scaffolds with designed porosity: experimental and computational analysis, *Mater. Sci. Eng. C* **70**, 812–823 (2017)
4. R. Wauthle, B. Vrancken, B. Beynaerts et al., Effects of build orientation and heat treatment on the microstructure and mechanical properties of selective laser melted Ti6Al4V lattice structures, *Addit. Manufactur.* **5**, 77–84 (2015)
  5. Z. Xu, A.N. Liu, X. Wang, B. Liu, M. Guo, Fatigue limit prediction model and fatigue crack growth mechanism for selective laser melting Ti6Al4V samples with inherent defects, *Int. J. Fatigue* **143**, 106008 (2021)
  6. W. Liu, C. Chen, S. Shuai, R. Zhao, L. Liu, X. Wang, T. Hu, W. Xuan, C. Li, J. Yu, J. Wang, Z. Ren, Study of pore defect and mechanical properties in selective laser melted Ti6Al4V alloy based on X-ray computed tomography, *Mater. Sci. Eng. A* **797**, 139981 (2020)
  7. B. Lxma, B. Ddba, B. Hija et al., Effects of embedded spherical pore on the tensile properties of a selective laser melted Ti6Al4V alloy, *Mater. Sci. Eng. A* **815**, 141254 (2021)
  8. K. Wei, F. Li, G. Huang, M. Liu, J. Deng, C. He, X. Zeng, Multi-laser powder bed fusion of Ti–6Al–4V alloy: defect, microstructure, and mechanical property of overlap region, *Mater. Sci. Eng. A* **802**, 140644 (2021)
  9. S. Tsopanos, R.A.W. Mines, S. Mckown, Y. Shen, W.J. Cantwell, W. Brooks, C.J. Sutcliffe, The influence of processing parameters on the mechanical properties of selectively laser melted stainless steel microlattice structures, *J. Manufactur. Sci. Eng.* **132**, 041011 (2010)
  10. R. Olaf, G. Bachmann Friedrich, E. Claus et al., Rapid manufacturing of lattice structures with selective laser-melting, *Laser-Based Micropackag.* 6017 61070K (2006). <https://doi.org/10.1117/12.645848>
  11. S. Zhang, X. Shubo, P. Yuefei et al., Mechanism study of the effect of selective laser melting energy density on the microstructure and properties of formed renewable porous bone scaffolds, *Metals* **12** (10) 1712 (2022).
  12. W. Zhuqing, D. Erik, M. Panagiotis et al., Residual stress mapping in Inconel 625 fabricated through additive manufacturing: method for neutron diffraction measurements to validate thermomechanical model predictions, *Mater. Des.* **113**, 169–177 (2017)
  13. M. Peter, K. Jean-Pierre, Residual stresses in selective laser sintering and selective laser melting, *Rapid Prototyp. J.* **12**, 254–265 (2006)
  14. K. Mahyar, G. Amirhossein, L. Martin et al., The effect of absorption ratio on melt pool features in laser-based powder bed fusion of IN718, *Optics & Laser Technology.* 153 108263 (2022).
  15. S. Xu, S. Zhang, G. Ren et al., Optimization of structural and processing parameters for selective laser melting of porous 316L bone scaffolds, *Materials* **15** (17) 5896 (2022).
  16. H.E. Ali, G. Shengmin, R. Jonathan, Corrosion performance of additively manufactured stainless steel parts: a review, *Addit. Manufactur.* **37**, 101689 (2021)
  17. V. Cruz, Q. Chao, N. Birbilis et al., Electrochemical studies on the effect of residual stress on the corrosion of 316L manufactured by selective laser melting, *Corros. Sci.* 164 108314 (2020).
  18. B. Xu, L. Kee-Won, L. Wenjie et al., A comparative study on cylindrical and spherical models in fabrication of bone tissue engineering scaffolds: finite element simulation and experiments, *Mater. Des.* **211**, 110150 (2021)
  19. G. Orhan, S. Ugur, C. Okan et al., Effect of build parameters on the compressive behavior of additive manufactured CoCrMo lattice parts based on experimental design, *Metals* **12**, 104 (2022)
  20. M. Peter, K. Jean-Pierre, Residual stresses in selective laser sintering and selective laser melting, *Rapid Prototyp. J.* **12**, 254–265 (2006)
  21. L. Bartlett Jamison, P. Croom Brendan, B. Jeffrey et al., Revealing mechanisms of residual stress development in additive manufacturing via digital image correlation, *Addit. Manufactur.* **22**, 1–12 (2018)
  22. A. Cuadrado, A. Yáñez, O. Martel et al., Influence of load orientation and of types of loads on the mechanical properties of porous Ti6Al4V biomaterials, *Mater. Des.* **135**, 309–318 (2017)
  23. J. Lv, Z. Jia, J. Li et al., Electron beam melting fabrication of porous Ti6Al4V scaffolds: cytocompatibility and osteogenesis, *Adv. Eng. Mater.* **17**, 1391–1398 (2015)
  24. N. Taniguchi, S. Fujibayashi, M. Takemoto et al., Effect of pore size on bone ingrowth into porous titanium implants fabricated by additive manufacturing: an in vivo experiment, *Mater. Sci. Eng. C* **59**, 690–701 (2016)
  25. L.E. Murr, Open-cellular metal implant design and fabrication for biomechanical compatibility with bone using electron beam melting, *J. Mech. Behav. Biomed. Mater.* **76**, 164–177 (2017)
  26. Y.F.K. Ueda, M. Tanigawa, New measuring method of 3-dimensional residual stresses based on theory of inherent strain, *J. Jpn. Soc. Naval Archit. Ocean Eng.* **145**, 203–211 (1979)
  27. P. Mercelis, J.P. Kruth, Residual stresses in selective laser sintering and selective laser melting, *Rapid Prototyp. J.* **12**, 254–265 (2006)
  28. W. Zhuqing, D. Erik, M. Panagiotis et al., Residual stress mapping in Inconel 625 fabricated through additive manufacturing: method for neutron diffraction measurements to validate thermomechanical model predictions, *Mater. Des.* **113**, 169–177 (2017)
  29. L. Bartlett Jamison, P. Croom Brendan, B. Jeffrey et al., Revealing mechanisms of residual stress development in additive manufacturing via digital image correlation, *Addit. Manufactur.* **22**, 1–12 (2018)
  30. S. Paul, K. Sören, K. Nikolai et al., Influence of laser shock peening on the residual stresses in additively manufactured 316L by laser powder bed fusion: a combined experimental-numerical study, *Addit. Manufactur.* 60 103204 (2022).
  31. J. Hua-Zhen, L. Zheng-Yang, F. Tao et al., Effect of process parameters on defects, melt pool shape, microstructure, and tensile behavior of 316L stainless steel produced by selective laser melting, *Acta Metall. Sin. (English Letters)* **34**, 495–510 (2020)
  32. G. Shaaz, B. Sarat, N. Kenneth et al., The influence of laser parameters, scanning strategies and material on the fatigue strength of a stochastic porous structure, *Addit. Manufactur.* **22**, 290–301 (2018)
  33. K.D. Ralston, N. Birbilis, C.H.J. Davies, Revealing the relationship between grain size and corrosion rate of metals, *Scr. Mater.* **63**, 1201–1204 (2010)
  34. A.-M. Nahid Sultan, M. Deen Kashif, H. Waseem et al., Corrosion behavior and biocompatibility of additively manufactured 316L stainless steel in a physiological environment: the effect of citrate ions, *Addit. Manufactur.* **34**, 101237 (2020)
  35. C. Qi, C. Victor, T. Sebastian et al., On the enhanced corrosion resistance of a selective laser melted austenitic stainless steel, *Scr. Mater.* **141**, 94–98 (2017)

36. H. Eftefagh Ali, G. Shengmin, R. Jonathan, Corrosion performance of additively manufactured stainless steel parts: a review, *Addit. Manufactur.* **37**, 101689 (2021)
37. O. Takakuma, H. Soyama, Effect of residual stress on the corrosion behavior of austenitic stainless steel, *Adv. Chem. Eng. Sci.* **5**, 62–71 (2015)
38. X.P. Tan, Y.J. Tan, C.S.L. Chow et al., Metallic powder-bed based 3D printing of cellular scaffolds for orthopaedic implants: a state-of-the-art review on manufacturing, topological design, mechanical properties and biocompatibility, *Mater. Sci. Eng. C* **76**, 1328–1343 (2017)

**Cite this article as:** Sen Zhang, Shubo Xu, Wei Zheng, Juanjuan Han, Study of the effect of SLM energy density on residual stress and microstructure of porous bone scaffolds in cubic structures, *Int. J. Simul. Multidisci. Des. Optim.* **13**, 23 (2022)